Appendix A

Procedures of Doing Time-Distance Measurement

This appendix is complimentary to Chapter 2, in which I have described the detailed procedures of doing time-distance measurement and inversion. I present in this appendix some part of the scripts, codes, and important parameters that I used in my study, so that readers of this dissertation may be able to repeat all the work included in this dissertation.

A.1 Data Preparation

It is strongly recommended that time-distance analysis be done on the central region of the solar disk, so that the side-effects caused by the large image distortion in limb regions may be limited to the minimum. Once the region of interest and the time period are decided, one should determine the Carrington longitude and latitude of the center of this region, as well as the MDI time index that the time period of interest corresponds to. To convert the real time of observation to the corresponding MDI time index, `time_index` is a useful command.

In order to perform FFT effectively, I often select a solar region with a size 256×256, and an observation duration of 512 minutes. Assume that we are analyzing a region with its center located at Carrington longitude of $100°$ and latitude of $10°$

in the northern hemisphere. The time period we are analyzing is from 00:00UT to 08:31UT on January 1, 2000. Running the command `time_index`, we can get

```
csh> time_index in=61344
hour 2000.01.01_00:00:00_TAI 3680640 61344 2556 1325376000.000 10224 85
```

Then we know that the corresponding MDI hour indices for our analysis period are from 61344 to 61351. Suppose that the datasets are from MDI full-disk observation. The script we run to track the region of interest and remap the region by utilizing Postel's projection is like the following:

```
!setenv mdi /tmp01/junwei/data_proc
p=fastrack d=1 \
  in=prog:mdi,level:lev1.5,series:fd_V_01h[61344-61351],sel:[00-31] \
  out=prog:mdi,level:lev2_track,series:vtrack_15_30_720[0] \
  scale=0.12 \
  rows=256 cols=256 \
  lat=10.0 lon=100.0 map=Postels \
  a0=0.0 a2=0.0 a4=0.0\
  n=0 z=0 v=1
```

The first line in the script is to provide a working directory where the final data are stored. The line with `a0, a2 and a4` is to give a rotation rate to be removed during the tracking procedure. To assign all these three values to be 0 is what I normally use, i.e., the solid Carrington rotation rate is removed from the data for all latitudes. Different tracking rate may be used by changing values of `a0, a2 and a4`. The argument `map=Postels` indicate that the mapping projection used is Postel's projection, whereas other projections, such as "rectangular", "orthographic", may be used. The dataset is then ready for time-distance analysis after the mean image of all these 512 images is removed from each image.

A.2 Filtering

As introduced in Chapter 2, two filters are usually applied on the dataset in the Fourier domain. One is to filter out the f-mode and all signals below the f-ridge, and the equations for the filter are given in equation 2.2; the other is the phase-velocity filter.

The choices of phase-velocity filter parameters, including the annulus ranges, the ratio of k/ω and the Full Width at Half Maximum (FWHM) of the Gaussian curve, are essential to the accuracy of the computed travel times. All through this dissertation, I used eleven annuli for computation of time-distance, and in Table A.1, I present all the parameters used in the computation.

	Annulus Range	k/ω Ratio	FWHM
1	$0^\circ.306$ - $0^\circ.714$	2.92	1.00
2	$0^\circ.510$ - $0^\circ.918$	3.40	1.00
3	$0^\circ.714$ - $1^\circ.190$	4.00	1.00
4	$1^\circ.190$ - $1^\circ.598$	5.675	1.47
5	$1^\circ.598$ - $2^\circ.414$	8.11	2.00
6	$2^\circ.176$ - $2^\circ.856$	9.08	1.16
7	$2^\circ.652$ - $3^\circ.400$	9.90	1.20
8	$3^\circ.196$ - $3^\circ.876$	10.90	1.36
9	$3^\circ.638$ - $4^\circ.454$	11.95	1.70
10	$4^\circ.182$ - $4^\circ.930$	13.07	1.44
11	$4^\circ.692$ - $5^\circ.372$	13.98	1.30

Table A.1: Parameters used to perform the phase-velocity filtering. Units for k/ω ratio and FWHM are both m/s.

A.3 Cross-Correlation and Fitting

Following equation 2.3, the discrete equations used to compute the cross-covariance between two signal series are:

$$r_{xy}(L) = \begin{cases} \dfrac{1}{N} \displaystyle\sum_{k=0}^{N-L-1} (x_{k+L} - \bar{x})(y_k - \bar{y}) & \text{for} L < 0 \\ \dfrac{1}{N} \displaystyle\sum_{k=0}^{N-L-1} (x_k - \bar{x})(y_{k+L} - \bar{y}) & \text{for} L \geq 0 \end{cases} \tag{A.1}$$

where x and y are the two signal series, L is time lag with both positive and negative values, and $r_{xy}(L)$ is the resultant cross-covariance function. IDL subroutine c_correlate.pro can be called directly for such a computation:

```
r = C_CORRELATE(x, y, L, /COVARIANCE)
```

As pointed out in §2.1, the IDL function lmfit.pro, a function to perform non-linear least squares fitting, can be used to fit the Gabor function obtained from the cross-correlation. The following is a sample IDL code to do the fitting:

```
FUNCTION myfunct, x, a

bx=EXP(-a(1)^2/4.*((x-a(2))^2))
cx=COS(a(3)*(x-a(4)))
RETURN,[[a(0)*bx*cx], [bx*cx], $
       [-0.5*a(0)*a(1)*((x-a(2))^2)*bx*cx], $
       [a(0)*bx*cx*(x-a(2))*(a(1)^2)/2.], $
       [a(0)*bx*(x-a(4))*(-SIN(a(3)*(x-a(4))))], $
       [a(0)*bx*a(3)*SIN(a(3)*(x-a(4)))]]

END

PRO lmqt_0, r, bb

x=FINDGEN(19)+2.
dat=FLTARR(19)
dat=r(101:119)/max(r)
aa=[1.0, 0.2, 10.5, 1.5, 12.1]
coefs=LMFIT(x, dat, aa, FUNCTION_NAME='myfunct',TOL=1.e-6,ITMAX=35)
bb=aa(4)

RETURN
END
```

The parameters of r and aa should be changed accordingly for different annulus ranges.

Certainly, the subroutines `c_correlate.pro` and `lmfit.pro` provided by IDL are not computational efficient in practice. Both of these two subroutines were translated into *FORTRAN* to meet the requirement of a large number of computations.

Appendix B

Deep-Focus Time-Distance

B.1 Deep-focus Time-Distance Measurement

Throughout this dissertation before this appendix, when we talk about time-distance, we mean surface-focus time-distance. As we know, more measurements can help to improve the accuracy of inversion results. Deep-focus time-distance was designed to meet such a requirement, and at the same time, bring up more information from the deeper layers of the solar interior.

As shown in the schematic plot of Figure B.1, surface-focus time-distance has the central point at the solar surface, hence it is like that its "focus" is at the surface, while deep-focus time-distance has its "focus" somewhere beneath the surface. Presumably, deep-focus should be more accurate in determining the deeper structures and dynamics. For the deep-focus scheme, by moving one set of rays to the left or to the right, one can move the "focus" point up or down. Therefore, one can design optimal schemes combining both surface- and deep-focus measurements to cover all the depths of interest in order to get better inversion results.

Basically, the procedure of performing deep-focus time-distance measurement is similar to that of surface-focus time-distance, except that for the surface-focus, we only have one central point, while for the deep-focus, we have an annulus of many points. Filtering, cross-correlation computation, and fitting subroutines are all the same, or sometimes with only slight modifications from surface-focus subroutines.

Figure B.1: A schematic plot to show the surface- and deep-focus time-distance measurement schemes.

An attempt has been made to combine both surface- and deep-focus time-distance measurements to study the subsurface dynamics of a sunspot. High resolution MDI observations of NOAA AR9236 on November 24, 2000 were selected for such an attempt. Eleven surface-focus measurements with different annulus ranges were performed based on the parameters given in Appendix A, and nine sets of deep-focus measurements were performed. All the necessary parameters to perform the deep-focus measurements are given in Table B.1. Please note that these parameters are just from one of my attempts to do deep-focus time-distance measurements. They are perhaps inaccurate, and probably, the choices of inner and outer annulus ranges are not optimal. Clearly, further efforts should be put into optimizing the measurement

	Inner Annulus Range	Outer Annulus Range	k/ω Ratio (m/s)
1	0°.136 - 0°.204	0°.544 - 1°.020	4.00
2	0°.306 - 0°.374	0°.850 - 1°.258	5.675
3	0°.578 - 0°.644	1°.054 - 1°.802	8.11
4	0°.918 - 0°.986	1°.190 - 1°.938	9.08
5	1°.122 - 1°.190	1°.462 - 2°.278	9.90
6	1°.326 - 1°.394	1°.802 - 2°.550	10.90
7	1°.530 - 1°.598	2°.074 - 2°.890	11.95
8	1°.734 - 1°.870	2°.414 - 3°.162	13.07
9	1°.938 - 2°.074	2°.686 - 3°.434	13.98

Table B.1: Parameters, including the inner and outer annuli ranges, and k/ω ratios, for the deep-focus time-distance measurements.

schemes, as discussed in Chapter 9.

B.2 Inversion Combining Surface- and Deep-Focus

It is interesting to see whether the combination of both surface- and deep-focus time-distance measurements can improve the inversion results, and how the inversion results compare with the previous inversions based on the surface-focus measurements only.

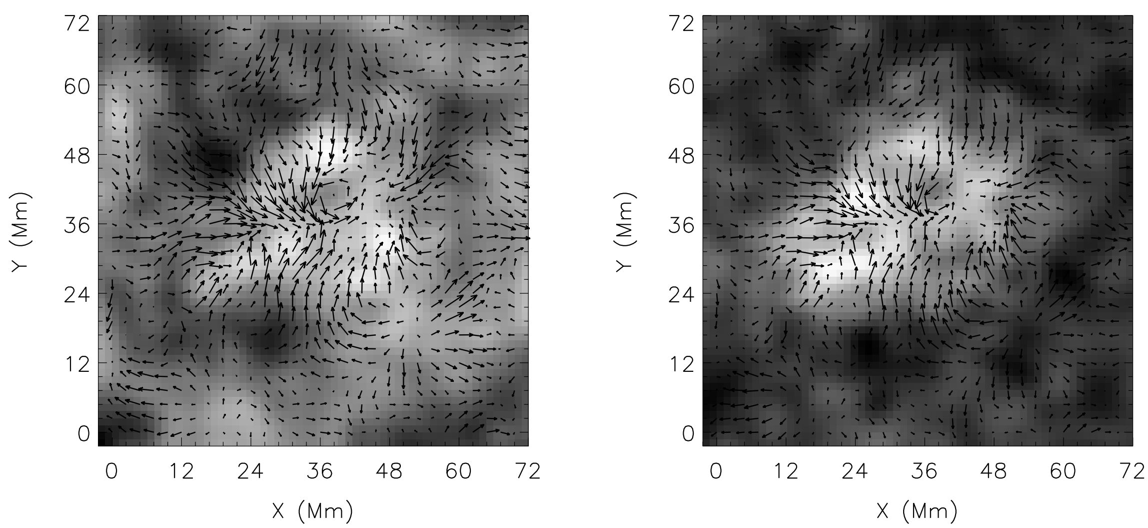

Figure B.2: Inversion results at the depth of $0-3$ Mm for AR9236 from surface-focus measurements alone (*left*) and from the combination of surface- and deep-focus measurements (*right*). The background images show the vertical velocity with light color representing downward flows, and vectors show the horizontal velocity after a 2×2 rebin.

The inversion kernels for the deep-focus measurements were also derived based on the ray-approximation, like for the surface-focus measurements described in Chapter 2.

Combining both surface- and deep-focus measurements, inversions were performed by use of LSQR algorithm. Inversions were also performed by use of surface-focus measurements alone by the same inversion technique. Results obtained from both approaches at the depth of $0-3$ Mm and at the depth of $6-9$ Mm are shown in

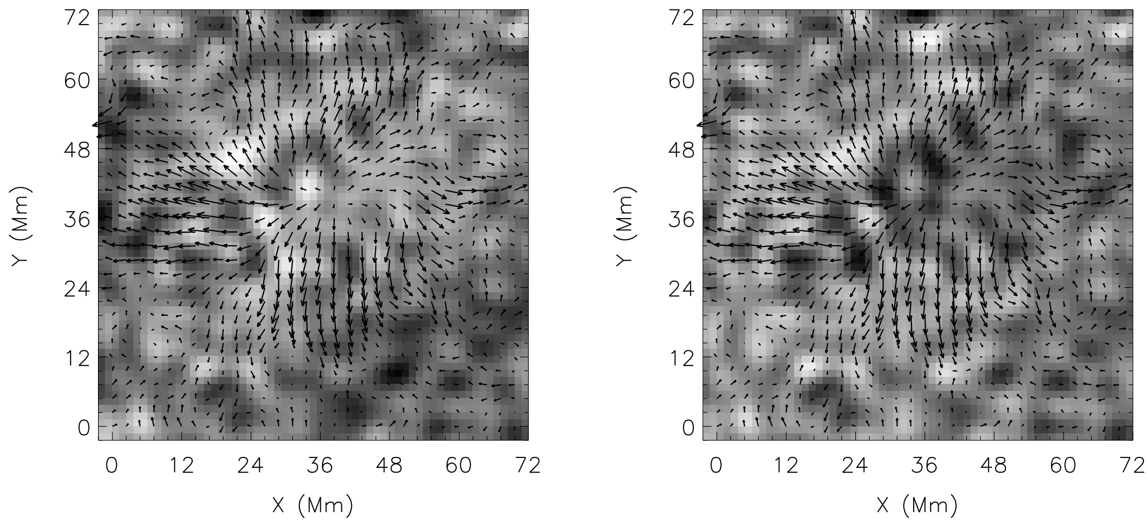

Figure B.3: Same as Figure B.2, but for the depth of 6 – 9 Mm.

Figure B.2 and B.3, respectively.

It can be obviously seen that basically, results from the both inversion approaches agree with each other, although the details differ from slightly to significantly at different locations. Near the surface, both inversions show downdrafts and converging flows toward the umbra of the sunspot. The vortex structure located at the center of the sunspot is seen in both inversions. At the depth of 6 – 9 Mm, both inversions show strong outflows from the sunspot, but the vertical flows differ significantly: results from the combination show clearly upward flows while results from surface-focus alone show somewhat mixed upward and downward directed flows.

At present, it is hard to discern whether one inversion is superior to the other, because the deep-focus measurement are still at its initial stage, and especially, the measurement scheme design used in this study is somewhat arbitrary, perhaps far from its optimal form. On the other hand, although it is proved that the ray-approximation kernels agree well with the wave-approximation kernels for the surface-focus time-distance inversions (Couvidat et al., 2004), it is not yet known whether the application of ray-approximation kernels on the deep-focus inversion is suitable. Additionally, from the measurements I made, it is obvious that the deep-focus measurements have larger noise level than the surface-focus ones. Then there is difficulty in choosing an optimal damping coefficient input for the LSQR to balance the different noise contributions from both sets of measurements. This factor may also play a role in the differences between inversion results.

Undoubtedly, for the purpose to study deeper areas of the Sun more reliably, deep-focus time-distance must be better developed in the future with the measurement schemes better designed to cover all depths. At the same time, wave-approximation inversion kernels for the deep-focus time-distance helioseismology should be developed as well.